

Spin-glass behavior in $K_xRu_{4-y}Ni_yO_8$ hollandite materialsLaura J. Vera Stimpson,¹ Jessica M. Powell,² Gavin B. G. Stenning,² Marek Jura,² and Donna C. Arnold¹¹*School of Physical Sciences, University of Kent, Canterbury, Kent, CT2 7NH, United Kingdom*²*ISIS Neutron and Muon Source, Rutherford Appleton Laboratory, Harwell Science and Innovation Campus, Didcot, OX11 0QX, United Kingdom*

(Received 31 July 2018; published 26 November 2018)

We report the synthesis and comprehensive ac and dc susceptibility measurements of $K_xRu_{4-y}Ni_yO_8$ hollandite. The value of the relative frequency shift, δT_f , has been determined as 0.025 which is within the range expected for spin-glass systems (0.005–0.06). Additionally, the characteristic flipping time of a single spin flip, τ_0 , and the dynamical critical exponent, $-zv$, were determined to have values of 5.82×10^{-8} s and 6.1(3), respectively from the power law. While the value of τ_0 is comparatively very large, $-zv$ is consistent with what is expected for spin-glass systems. Field-cooled hysteresis behavior demonstrates a small increase in the remnant magnetization (at 2 K) on increasing the strength of the cooling field, suggesting that the degree of short-range correlations increases consistent with the formation of larger spin clusters. Thermoremanent magnetization data indicate an exponential-like decay of the magnetization as a function of time with the remnant magnetization remaining nonzero. However, it is clear from these data that multiple components contribute to the decay behavior. Collectively, these data confirm spin-glass character for $K_{0.73(3)}Ni_{1.9(5)}Ru_{2.1(5)}O_8$ and clearly demonstrate that the magnetic behavior of this material is far from simplistic.

DOI: [10.1103/PhysRevB.98.174429](https://doi.org/10.1103/PhysRevB.98.174429)**I. INTRODUCTION**

The hollandite family (general formulae $A_xM_8O_{16}$, where A is typically an alkali or alkaline earth metal and M is a transition metal) offers an exciting and flexible platform for the investigation of complex behaviors. For example extensive studies have been performed investigating hollandite materials for application in molecular sieves (e.g., Ref. [1]), catalysts (e.g., Ref. [2]), and in battery technologies (e.g., Ref. [3]). The hollandite structure can be described as a network of MO_6 octahedral units which share both corners and edges to form a 2×2 network of octahedra in the crystallographic a/b plane [4]. These octahedral units are edge shared in the lattice c direction to form “zigzag” chains as shown in Fig. 1. The A cation sits in the tunnels formed within the MO_6 framework. These materials typically crystallize with either tetragonal ($I4/m$) or monoclinic ($I2/m$) symmetry dependent on the size of the A and M cations [5]. Incorporation of magnetic ions on to the MO_6 framework can lead to interesting magnetic behavior but in comparison with other potential applications magnetism in these materials have received far less attention [6]. Recently, Larson *et al.* related the hollandite structure to geometrically frustrated triangular lattices whereby the hollandite topography can be thought of to arise from rolling infinite MO_6 layers to form 1D tubes [4]. This is exciting as geometric frustration, where magnetic interactions are incompatible with the underlying crystal structure, have been shown to lead to unusual magnetic ground states. Larson *et al.* demonstrated control of the magnetic properties in $Ba_{1.2}Mn_8O_{16}$ through doping of the Mn site with Co [4]. The parent $Ba_{1.2}Mn_8O_{16}$ material exhibits a complex antiferromagnetic spin arrangement below T_N (25 K) where four unique spin arrangements result

in a modulated helical structure which spatially averages to zero. The addition of Co^{2+} to the framework disrupts the helical order, giving rise to a ferrimagnetically ordered state with a greatly increased transition temperature, T_C , of 180 K [4]. The same group also investigated the magnetic behavior of $Bi_{1.7}V_8O_{16}$ and Sc to Ni doped (denoted by M) $K_xTi_{8-y}M_yO_{16}$ materials [7–9]. All $K_xTi_{8-y}M_yO_{16}$ materials exhibited Curie paramagnetism consistent with the limited amounts of magnetic species incorporated into these materials [8]. In contrast, while the $Bi_{1.7}V_8O_{16}$ material exhibits no long-range magnetic order, as observed by powder neutron diffraction, magnetotransport measurements suggest a dimerization of the mixed spin cations [7]. Multi-ferroic character has also been reported in $BaMn_3Ti_4O_{14.25}$ hollandite [10,11]. In this material charge order results in the Mn^{4+} , Mn^{3+} , and Ti^{4+} being ordered on crystallographically distinct sites and the observation of long-range antiferromagnetic order and ferroelectric switching [10,11].

Materials that contain $4d$ and $5d$ magnetic ions such as ruthenium and iridium are attracting extensive research interest due to the potential of these materials to exhibit exotic electronic and magnetic ground states. For example, spin triplet superconductivity has been reported for Sr_2RuO_4 , while metamagnetism and pseudo-gap formation have been reported for $Sr_3Ru_2O_7$ and $BaRuO_3$, respectively [12–15]. More recently, Ying *et al.* report ferromagnetic quantum criticality and non-Fermi liquid behavior in $La_4Ru_6O_{19}$ [16]. Given the complex magnetic ion connectivity in hollandites and the propensity of $4d$ ruthenate materials to exhibit interesting magnetic states it is not unreasonable to suggest that interesting phenomena may be realized in ruthenate hollandites. In fact, electronic measurements on $BaRu_6O_{12}$ single crystals demonstrated that the material was insulating

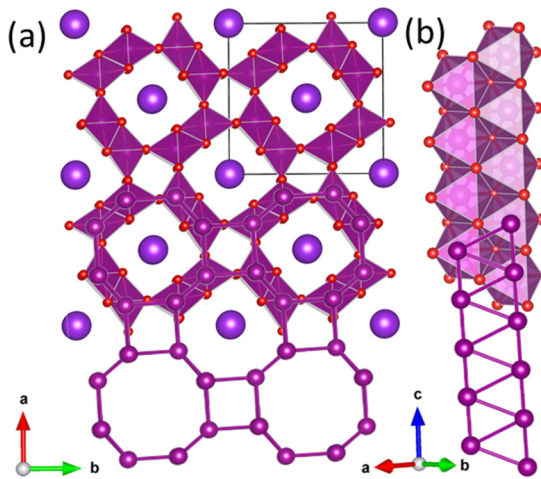


FIG. 1. Schematic representation of the hollandite, $A_xM_4O_8$, structure in the tetragonal $I4/m$ setting where (a) shows the 2×2 tunnels formed in the crystallographic a/b plane and (b) shows the edge shared MO_6 octahedral network in the crystallographic c direction. The pink spheres and squares represent the M ions and MO_6 octahedra, respectively. The purple spheres represent the A cations and the red spheres the oxygen ions.

and confirmed, at least electronically, the quasi-1D nature of the structure [17]. While no long-range order was observed in magnetometry data down to 2 K, the authors do, however, suggest (based on cooperative measurements) the presence of a quantum phase transition and the existence of a weakly localized ground state below 2 K [17]. Similar results have also been reported for KRu_4O_8 crystals [18]. Foo *et al.* reported that KRu_4O_8 , $RbRu_4O_8$, and $Ca_{0.8}Li_{0.2}Ru_4O_8$ are paramagnetic metals [19]. While the resistivity measurements were performed to a temperature of 0.3 K it is unclear what base temperature was used for the magnetometry measurements [19]. More recently, quasi-one-dimensional electron conduction has been suggested for KRu_4O_8 from density-functional theory (DFT) calculations [20–22]. These authors further suggested that KRu_4O_8 could be considered to be a Tomonaga-Luttinger liquid [22,23]. The influence of structural disorder in $A_xRu_4O_8$ hollandite materials has been investigated, where A is K, Rb, or a mixture of Na and Rb [24]. These authors reported that all materials exhibited an anisotropic resistivity which is dominated by metallic conductivity. All materials also exhibited Pauli paramagnetism over the temperature range of 5 to 300 K [24].

It is clear that our understanding of the properties of this class of ruthenium-based materials is still limited. Furthermore, the effect of doping these structures to control/tune the electronic and/or magnetic behavior has received almost no attention. In this paper we report the synthesis of a $K_xRu_{4-y}Ni_yO_8$ hollandite material. Crystallographic studies confirm the material adopts the tetragonal, $I4/m$ symmetry with Ni and Ru disordered across the MO_6 framework. Both ac and dc susceptibility measurements confirm the material behaves as a spin glass below T_N of approximately 28 K (at 0.1 T).

II. EXPERIMENTAL

Polycrystalline $K_xRu_{4-y}Ni_yO_8$ samples were prepared using hydrothermal methods. Briefly, a 2:3 ratio of $NiCl_2$ and $KRuO_4$ (both Sigma-Aldrich, >99%) were dissolved in distilled deionized H_2O (30 mL). The resulting solution was heated in a 45-mL Teflon-lined Parr cell for 24 h at 200 °C. The cell was placed into a preheated oven and cooled at a rate of 0.1 °C/min. The final product was filtered and washed with ddH_2O and dried at 60 °C for 24 h.

Phase purity was confirmed using the Rigaku MiniFlex 600 x-ray diffractometer (data not shown here). High-quality diffraction data were collected using a Rigaku SmartLab rotating anode $\theta/2\theta$ diffractometer using $Cu K\alpha$ radiation ($\lambda = 1.54413 \text{ \AA}$) operating at 45 kV and 200 mA (2θ range: 5–90°). Rietveld refinements were performed to obtain structural information using the GSAS suite of programs as described in more detail in Sec. III [25,26]. dc magnetic susceptibility measurements were collected using a Quantum Design Magnetic Property Measurement System MPMS-XL7 instrument under both zero-field-cooled (ZFC) and field-cooled (FC) environments over a temperature range of 1.8 to 300 K and applied magnetic fields (H) of between 0 and 7.0 T. Variable field hysteresis data were collected at temperatures between 2 and 300 K over an applied magnetic field range of –5 to 5 T. Compositional information was collected using a PANalytical Epsilon-3XL x-ray fluorescence spectrometer. ac susceptibility measurements were performed using a PPMS-9 Physical Property Measurement system. Data were collected at fixed frequencies of 100, 215, 464, 1000, 2154, and 2642 Hz in an applied field of 0.1 T over a temperature range of 2–100 K.

III. RESULTS AND DISCUSSION

Powder-diffraction studies confirmed the synthesis of the hollandite phase. However, we note the formation of a RuO_2 second phase in our materials. Repeated attempts to prepare materials without this impurity by changing both synthetic conditions and starting ratios failed to improve the hollandite phase purity. The structure of the hollandite materials was further investigated by performing Rietveld refinements using the GSAS suite of programs [25,26]. Refinements were first performed using the $I4/m$ model reported by Laurita *et al.* for $K_xRu_4O_8$ materials for 49 variables which included 12 background coefficients (fitted with a shifted Chebyshev function), lattice parameters, atomic positions, and fractional occupancies (for K, Ni, and Ru). The peak shape was fitted using a pseudo-Voigt relationship as described by Howard, and Thompson *et al.* [24,27,28]. The thermal parameters (U_{iso}) for the Ru and Ni ions were refined; however, the U_{iso} for the potassium and oxygen atoms were fixed at a value of $1.0 U_i/U_e^*100 \text{ \AA}^2$ as refinement led to nonsensible values due to insensitivity of laboratory-based x-ray instrumentation to light atoms. A secondary RuO_2 phase was also included in the refinement [refined to 27.3(5)%]. Good agreement between the tetragonal model and the data is observed as shown in Fig. 2 with refinement parameters given in Table I. Refinement of the fractional occupancies for the K, Ni, and Ru ions gives a nominal formula of $K_{0.43(1)}Ru_{2.04(2)}Ni_{1.96(2)}O_8$,

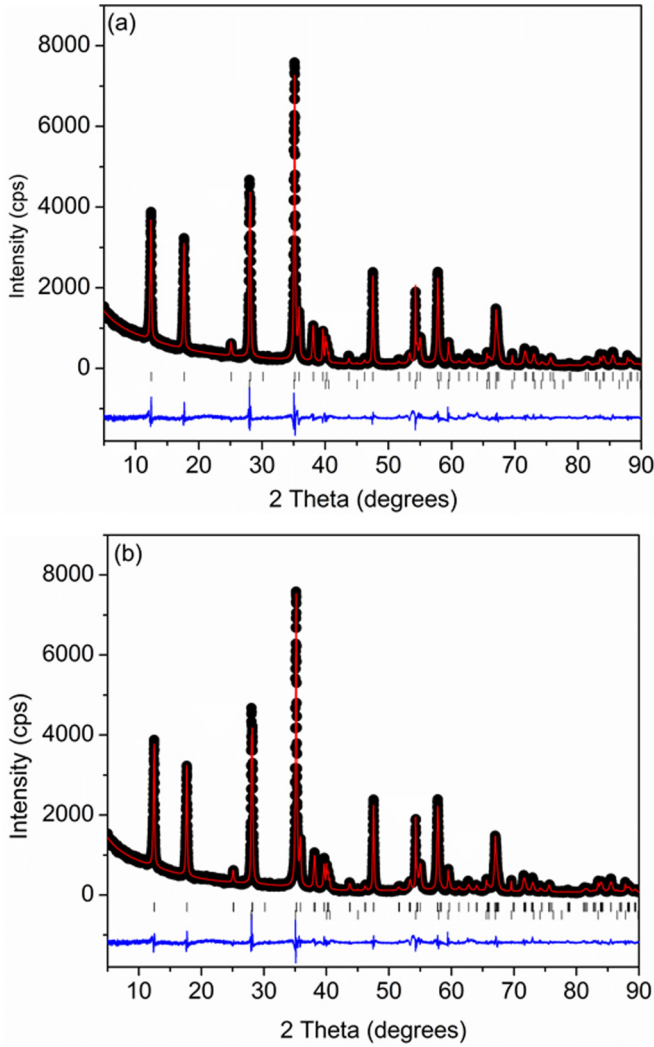


FIG. 2. Rietveld refinements of x-ray diffraction data collected for $K_xRu_{1-y}Ni_yO_8$ refined with (a) tetragonal, $I2/m$ and (b) monoclinic, $I4/m$ symmetry [24,29]. The black circles represent the observed data, the red line the calculated model, and the blue line is the difference curve. The top row of tick marks represents the reflections expected for the $K_xRu_{1-y}Ni_yO_8$ phase and the bottom row of tick marks represents the reflections expected for the RuO_2 impurity phase.

assuming no oxygen vacancies. Since hollandite materials can crystallize with either monoclinic or tetragonal symmetry we also considered the monoclinic, $I2/m$ model [29].

TABLE I. Rietveld refinement parameters determined from the refinement of x-ray diffraction data collected for $K_xRu_{1-y}Ni_yO_8$ (space group: $I4/m$). $\chi^2 = 3.718$, wRP = 9.24%, Rp = 6.46% [24].

Refinement parameters					
a (Å)	9.9980(2)	c (Å)	3.09659(7)	Cell vol. (Å ³)	309.51(1)
Atom positions	K	Ru/Ni	O1	O2	
X	0.000000	0.3428(2)	0.1200(1)	0.5459(1)	
Y	0.000000	0.1672(2)	0.191(1)	0.131(1)	
Z	0.500000	0.000000	0.000000	0.000000	
$U_{(iso)}/U_{(e)} \times 100$ (Å ²)	1.00	0.40(7)	1.00	1.00	
Fractional occupancy	0.43(1)	Ru = 0.51(2), Ni = 0.49(2)	1.0000	1.0000	

These refinements were performed as described above for the tetragonal model with 55 variables due to the extra degrees of freedom afforded by monoclinic symmetry. However, in all cases the U_{iso} were fixed at $1.0 U_i/U_e \times 100 \text{ Å}^2$ as refinement led to nonsensible values. The RuO_2 content was refined to 22.6(5)%. The refinement parameters and profile are given in Table II and Fig. 2, respectively. Lowering the symmetry from tetragonal to monoclinic affords two crystallographic distinct M sites, based on the general formulae $A_xM_8O_{16}$, which could potentially allow for site ordering of the Ni and Ru cations. Close inspection of the refined fractional occupancies for both Ni and Ru shows they are reasonably equally distributed across both crystallographic sites, suggesting the absence of any cation order in these materials (Table II). A nominal formula of $K_{0.473(8)}Ru_{1.8(2)}Ni_{2.2(2)}O_8$ has been determined from the refinement. The bond angles and bond lengths for both the tetragonal and monoclinic refinements are given in Table III. We note that the monoclinic refinement gives improved goodness-of-fit parameters over the tetragonal model and we have further considered these two models using the significance tests for crystallographic R factor as proposed by Hamilton [30]. The ratio of the R_{exp} goodness-of-fit factors is 1.107, using the tables provided by Hamilton, suggesting that the improved fit is not significant at the 95% confidence interval. We therefore suggest that the perceived improved fit for the monoclinic model arises solely as a result of the extra degrees of freedom present in monoclinic symmetry and thus $K_xRu_{4-y}Ni_yO_8$ crystallizes with tetragonal symmetry consistent with other ruthenate hollandites [18,19,24]. This is perhaps not surprising given geometric and cation size ratio considerations (in the absence of site ordering) as reported by Zhang *et al.* whereby monoclinic symmetry can only be satisfied when

$$r_A < \sqrt{2}(r_O + r_B) - r_O - 0.15, \quad (1)$$

where r_A , r_B , and r_O are the ionic radii of the A-site, B-site, and O cations, respectively [5]. In contrast, tetragonal symmetry can be expected when

$$r_A > \sqrt{2}(r_O + r_B) - r_O. \quad (2)$$

If we consider a 1:1 ratio of Ni^{3+} (ionic radii = 0.6 Å) and Ru^{4+} (ionic radii = 0.62 Å), as determined from our refinements, we obtain the values 1.30 and 1.45 Å for Eqs. (1) and (2), respectively. The ionic radii for K^+ , r_A , are given as 1.64 Å (12 coordinate); in this case we can see that r_A is far

TABLE II. Rietveld refinement parameters determined from the refinement of x-ray diffraction data collected for $K_xRu_{1-y}Ni_yO_8$ (space group: $I2/m$). $\chi^2 = 2.868$, wRP = 8.35%, Rp = 5.90% [29].

Refinement parameters							
a (Å)	9.9999(4)	b (Å)	3.09559(8)	c (Å)	9.9952(3)		
β (°)	90.148(5)	Cell vol. (Å ³)		309.41(2)			
Atom positions	K	Ru/Ni1	Ru/Ni2	O1	O2	O3	O4
x	0.00000	0.1600(3)	0.3442(3)	0.176(1)	0.123(2)	0.085(2)	0.508(2)
y	0.50000	0.000000	0.000000	0.000000	0.000000	0.000000	0.000000
z	0.00000	0.3410(4)	0.8304(3)	0.110(1)	0.790(1)	0.549(1)	0.816(1)
Fractional occupancy	0.473(8)	Ru = 0.37(2), Ni = 0.63(2)	Ru = 0.53(2), Ni = 0.47(2)	1.0000	1.0000	1.0000	1.0000

larger than both 1.30 and 1.45 Å and thus tetragonal symmetry should be expected.

In order to probe the possible composition of these materials further we performed x-ray fluorescence (XRF) spectroscopy. These measurements gave an approximate composition of $K_{0.73(3)}Ru_{2.1(5)}Ni_{1.9(5)}O_8$ taking into account RuO_2 at the percentage determined from the Rietveld refinements (in tetragonal symmetry) of the x-ray diffraction data. This Ru:Ni ratio is consistent with that determined from Rietveld refinement. We note however, a larger K content than that determined from refinements. Given difficulties in refining the U_{iso} for K in our refinements coupled with the insensitivities of x-ray diffraction experiments we believe the potassium content is most likely underestimated in our current refinements. The potassium content determined from the XRF experiments is also more closely aligned with the potassium/A-cation contents observed in other ruthenate hollandites [18,19,24]. If we assume no oxygen vacancies charge balance means we have nickel in the +3 oxidation state while ruthenium is mixed between +4 and +5 oxidation states.

ZFC and FC superconducting quantum interference device (SQUID) magnetometry data were collected between 2 and 380 K in an applied field of 0.1 T as shown in Fig. 3. The

 TABLE III. Selected bond lengths and bond angles determined from the Rietveld refinement of x-ray diffraction data collected for $K_xRu_{1-y}Ni_yO_8$ (space group: $I4/m$ and $I2/m$) [24,29].

Tetragonal, $I4/m$		Monoclinic, $I2/m$	
Parameter	Value	Parameter	Value
Ru1/Ni1-O1 (Å)	2.240(9)	Ru1/Ni1-O1 (Å)	2.31(2)
Ru1/Ni1-O1 \times 2 (Å)	2.133(6)	Ru1/Ni1-O1 \times 2 (Å)	2.306(9)
Ru1/Ni1-O2 (Å)	2.063(9)	Ru1/Ni1-O3 (Å)	2.22(1)
Ru1/Ni1-O2 \times 2 (Å)	1.985(6)	Ru1/Ni1-O4 \times 2 (Å)	2.180(9)
N/A	N/A	Ru2/Ni2-O2 (Å)	2.25(2)
N/A	N/A	Ru2/Ni2-O2 \times 2 (Å)	1.986(8)
N/A	N/A	Ru2/Ni2-O3 \times 2 (Å)	2.084(8)
N/A	N/A	Ru2/Ni2-O4 \times 2 (Å)	1.65(2)
Ru1-O1-Ru1 (°)	93.1(3)	Ru1-O4-Ru1 (°)	90.5(5)
Ru1-O2-Ru1 (°)	125.3(2)	Ru1-O4-Ru2 (°)	133.0(3)
Ru1-O2-Ru1 (°)	102.6(4)	Ru2-O2-Ru2 (°)	100.6(6)
N/A	N/A	Ru1-O3-Ru2 (°)	115.1(5)
N/A	N/A	Ru2-O3-Ru2 (°)	96.0(5)

data show a clear divergence between ZFC and FC data below ~ 28 K suggestive of spin-glass-like or ferrimagnetic behavior. RuO_2 , like many other $4d$ transition-metal oxides, has been reported to be a Pauli paramagnet with no long-range magnetic order [31]. More recently, Berlijn *et al.* have reported that RuO_2 is in fact an itinerant antiferromagnet with $T_N \geq 300$ K and a small magnetic moment of $0.05 \mu_B$ [32]. This manifests itself as a very subtle broad peak at high temperature in the susceptibility data with paramagnetic like behavior below 300 K. In this sense it is therefore unlikely that the low-temperature behavior observed in our susceptibility data arises as a result of the secondary RuO_2 phase and thus it can be considered to be characteristic of the $K_xRu_{4-y}Ni_yO_8$ hollandite material. Likewise, undoped $K_xRu_4O_8$ has been reported to exhibit paramagnetic like behavior with no anomalies observed in SQUID magnetometry data below room temperature [18,19,24]. This suggests that doping of the ruthenium site with nickel results in some degree of (short-range) magnetic order as evidenced by the spin-glass-like behavior observed in our SQUID magnetometry data (Fig. 3). This presumably arises as a result of cation disorder on the M site which is consistent with the model proposed by Crespo *et al.* which suggests that a combination of geometric frustration, antiferromagnetic nearest-neighbor interactions, and cation disorder are responsible for the evolution of spin-glass behavior in hollandite materials [33]. Fitting the Curie-Weiss law to these data between 200 and 300 K gives the expected linear fit [Fig. 3(b)]. From the equation of the straight line we have extracted values for the Weiss constant θ and the observed magnetic moment μ . A negative Weiss constant θ of -178.11 K is observed which is consistent with antiferromagnetic/ferrimagnetic or spin-glass character. From this fit a total magnetic moment of $4.8 \mu_B$ was also determined that is considerably lower than the calculated magnetic moment per formula unit, $8.1 \mu_B$. However, it is common for ruthenium containing oxides to show very low magnetic moments from Curie-Weiss fits and this may suggest that the effective magnetic moment is dominated by the Ni^{3+} ion [32,34]. We should also note that these data additionally contain a contribution from RuO_2 which may affect the calculations performed here. If we consider the relationship between the Weiss constant and the transition temperature T_N , which can be used to give an indication of the level of frustration in these materials as given in Eq. (3) (below), we get a value for the frustration index of 6.4 which suggests the material is heavily frustrated consistent with the 1D structural

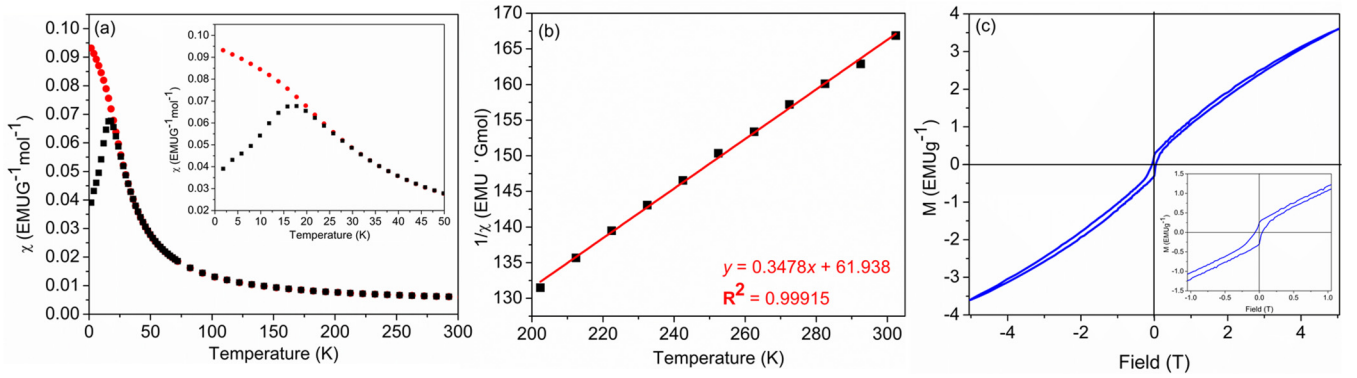


FIG. 3. dc susceptibility data collected at 0.1 T for $K_x\text{Ru}_{4-y}\text{Ni}_y\text{O}_8$ where (a) shows the zero-field-cooled (black squares) and field-cooled (red circles) data, (b) gives the temperature vs $1/\chi$ Curie-Weiss plot showing linear character giving a Weiss constant θ of -178.11 K and a total magnetic moment of $4.8 \mu_B$, and (c) shows the variable field data collected at 2 K showing weak hysteric behavior. Inset of (a) shows a zoomed-in region of the zero-field-cooled and field-cooled data showing more clearly the divergence between the data at approximately 28 K and the inset of (c) shows a zoomed-in region of the magnetization-field hysteresis loop showing the “pinched” nature of the loops obtained for these materials.

chains and the model proposed by Crespo *et al.* [33]:

$$f = \frac{-\theta_{CW}}{T_N}, \quad (3)$$

where f is the frustration index (where a value of 1 is expected for nonfrustrated spin order), θ_{CW} is the Weiss constant, and T_N is the transition temperature [35]. Variable-field data collected at 2 K exhibit weak hysteresis that does not saturate under the conditions investigated [Fig. 3(c)] consistent with spin-glass-like behavior. Close inspection of the data demonstrates that the loop is pinched similar to those reported for the antiperovskite, PdNCr_3 [36]. This is suggestive of cation disorder consistent with the diffraction data discussed above.

In order to further investigate the potential spin-glass-like behavior we have additionally performed variable-frequency ac susceptibility. The real $\chi'(T)$ and imaginary $\chi''(T)$ part of the ac susceptibility are shown in Fig. 4. There is a clear frequency dependence of the susceptibility in the $\chi'(T)$ data with a loss in peak intensity and a shift to higher temperatures of the spin-glass transition temperature T_f with increasing frequency consistent with other spin-glass systems. (e.g., Refs. [36–40]) In contrast, there is little frequency dependence in the $\chi''(T)$ data. However, $\chi''(T)$ is clearly nonzero below T_f , which is consistent with spin-glass behavior. We also note that the noise associated with these data may mask weak frequency dependence in our $\chi''(T)$ data. Information regarding the spin dynamics of the system and the strength of the spin interactions can be extracted from the frequency dependence of the transition temperature, T_f [given by the peak maxima in the $\chi'(T)$ data] as detailed in Eq. (4) [36,39]:

$$\delta T_f = \frac{\Delta T_f}{T_f \Delta(\log_{10} f)}, \quad (4)$$

where δT_f is the relative frequency shift and T_f is the transition temperature at a given frequency, f . From our data we calculate a value for δT_f of 0.025. This value falls within the expected range of between 0.005 and 0.06 typical of spin-glass systems as discussed in previous works [36,37,39,40]. Typically in spin-glass materials the relationship between

the relaxation time and the transition temperature can be described by the power law given in Eq. (5) [39]:

$$\tau = \tau_0 \left[\frac{T_f - T_{SG}}{T_{SG}} \right]^{-zv}, \quad (5)$$

where T_{SG} is the freezing temperature as the frequency tends to zero [determined as 18.7(1) K from a plot of T_f vs f as shown in Fig. 4(c)], τ_0 is the characteristic flipping time of a single spin flip, τ is the relaxation time as given by $1/f$, and $-zv$ is the dynamical critical exponent. Extracting the intercept and the slope gives values for τ_0 and $-zv$ of 5.82×10^{-8} s and 6.1(3), respectively. While the value of $-zv$ is in line with the values typically observed for spin-glass materials the value of τ_0 is far larger than the $10^{-11}/10^{-12}$ values expected [36,37,39,40]. Anand *et al.* also noted large values for τ_0 (2.04×10^{-10} s) in the intermetallic, PrRhSn_3 , which they attributed to strong spin correlations in clusters as opposed to the interactions of individual spins [39]. While our observations may also suggest slow spin dynamics arising as a result of either the formation of cation ordered clusters or strong spin correlations afforded by the complex nature of the mixed cation state we note that since these values are determined ultimately from the interpretation of T_f from the frequency-dependent $\chi'(T)$ data and T_{SG} from the extrapolation of the linear relationship of T_f with frequency there is propensity for error. In real terms it is unlikely that error alone can account for the high value of τ_0 and it is likely that these results do indeed suggest some level of strong spin correlation in these materials. Furthermore, while unlikely, we cannot rule out that the secondary RuO_2 phase may additionally contribute to this larger than expected value. When investigating spin-glass systems further information about spin dynamics can also be determined from the Arrhenius relationship [Eq. (6)] and Vogel-Fulcher law [Eq. (7)].

$$f = f_0 \exp\left(-\frac{E_a}{k_B T_f}\right), \quad (6)$$

$$f = f_0 \exp\left(\frac{E_a}{k_B (T_f - T_0)}\right), \quad (7)$$

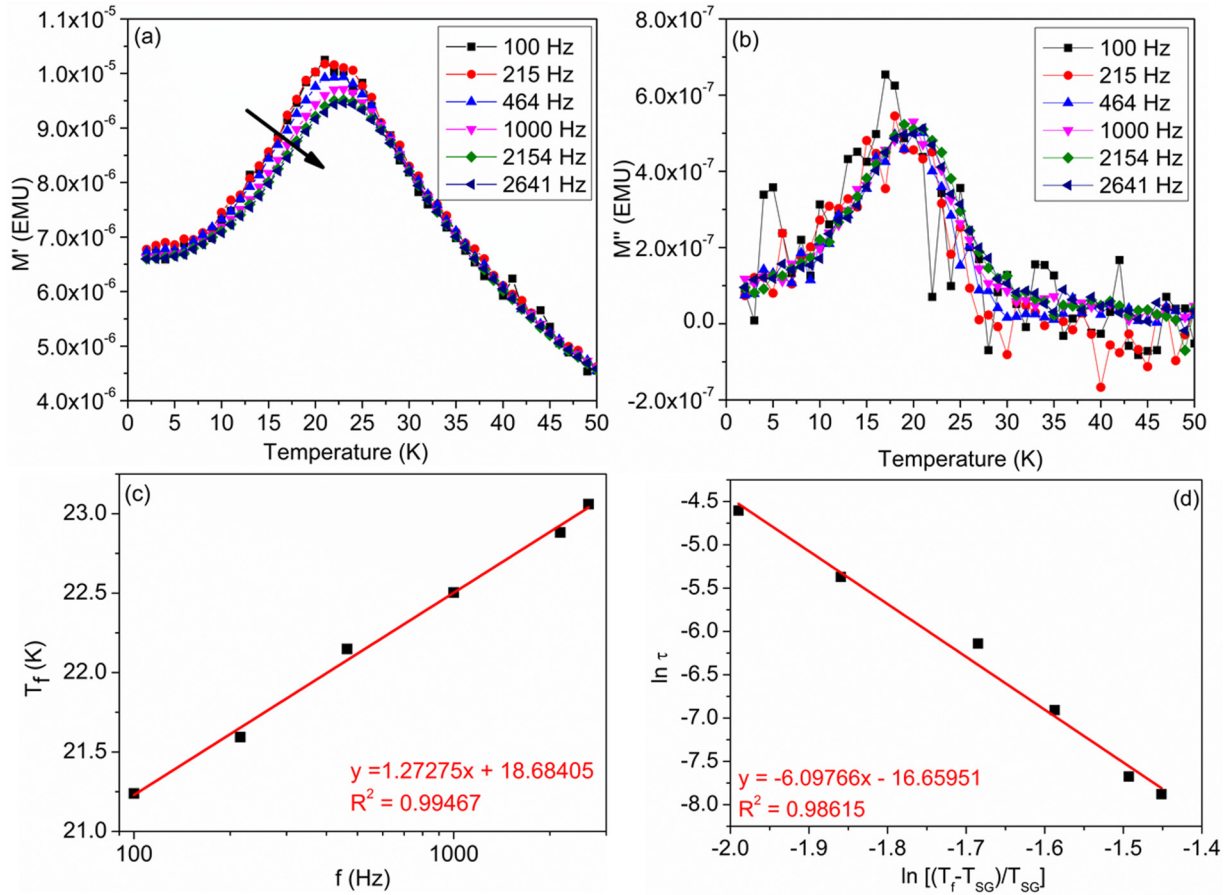


FIG. 4. (a) Real $\chi'(T)$ and (b) imaginary $\chi''(T)$ parts of the ac susceptibility as a function of temperature and frequency (applied ac field of 0.1 T) showing spin-glass-like behavior and frequency dependence of the freezing temperature T_f plotted (c) as a function of frequency where the linear fit allows the intercept T_{SG} to be determined and (d) as $\ln \tau$ vs $\ln[(T_f - T_{SG})/T_{SG}]$ with the linear fit representing the fit to the power law allowing for the determination of $\ln \tau_0$ (intercept) and $-zv$ (slope).

where f_0 is the fundamental attempt or limiting response frequency of the spins, E_a is the activation energy, T_0 is the Vogel-Fulcher temperature, and k_B is Boltzmann's constant ($1.381 \times 10^{-23} \text{ J K}^{-1}$). Figure 5(a) shows the linear plot of $\ln f$ vs $1/T_f$; typically a linear Arrhenius relationship is indicative of weakly or noninteracting spins [37]. For example, Anand *et al.* saw a deviation from linearity at low frequencies which they attributed to the formation of strongly interacting clusters [39]. We note that despite the large values of τ_0 observed for our materials from the fit to the power law we see no evidence of a deviation from linearity to support the formation of strongly correlated clusters. However, the lowest frequency we collected our data at is $f = 100 \text{ Hz}$ and thus we cannot rule out the formation of such clusters from our measured frequency range. From the equation of the straight line we have extracted values of $1.1 \times 10^{20} \text{ Hz}$ and $882(32) \text{ K}$ for f_0 and E_a/k_B , respectively. Both values are physically unrealistic with f_0 expected to be on the order of 10^{12} Hz . The observation of unrealistic values from Arrhenius plots is not uncommon, however, and both Bakaimi *et al.* and Anand *et al.* reported unrealistic values of f_0 and E_a/k_B from Arrhenius plots for $\text{Na}_x\text{MnO}_2 \cdot y\text{H}_2\text{O}$ and PrRhSn_3 materials [37,39]. Fitting of the Vogel-Fulcher to determine f_0 , E_a , and T_0 proved difficult due to the limited frequency range that the

data have been collected over, meaning it is impossible to fit the expected curve to the data. We have seen similar problems in dielectric relaxor data whereby unrealistic values are obtained as a result of the sensitivity of fitting to the curvature of $Tm(f)$ data and subsequently extrapolating over several orders of magnitude [41]. We have therefore adopted the method outlined by Anand *et al.* in order to try and estimate values for these parameters [39]. They employed two different methodologies; the first was to assume a value of the attempt frequency such that $f_0 = 1/\tau_0$ with the value of τ_0 taken to be that determined from the power-law fit. Values for E_a/k_B and T_0 can then be determined from the slope and intercept of the linear relationship between T_f and $100/\ln(f_0/f)$ and given by Eq. (8). Secondly, in order to investigate if the values of E_a/k_B and T_0 have been biased by the assumption of the value of f_0 , they determined a value of T_0 based on the method outlined previously [39,42]. Subsequently plotting $\ln f$ versus $1/(T_f - T_0)$ allows for E_a/k_B and f_0 to be determined from the slope and the intercept, respectively [Eq. (9)]:

$$T_f = \frac{E_a/k_B}{\ln(f_0/f)} + T_0, \quad (8)$$

$$\ln f = \ln f_0 - \frac{E_a/k_B}{T_f - T_0}. \quad (9)$$

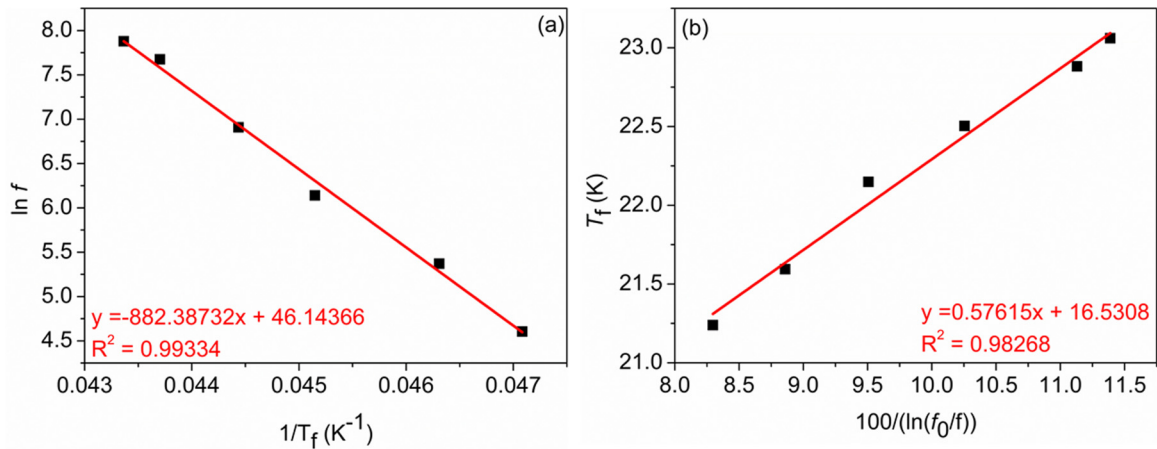


FIG. 5. (a) Arrhenius fit of the frequency as a function of the freezing temperature ($1/T_f$ vs $\ln f$) and (b) Vogel-Fulcher fit of the frequency as a function of the freezing temperature [$100/(\ln(f_0/f))$ vs T_f] assuming $f_0 = 5.82 \times 10^{-8}$ s.

Using the value of τ_0 (5.82×10^{-8} s) as determined from the power law we have determined values of E_a/k_B and T_0 as 0.58(3) and 16.5(3) K, respectively [Fig. 5(b)]. We note that these values are most likely compromised by the higher value of τ_0 extracted from our fits. Attempts to determine T_0 and thus use the modified Vogel-Fulcher equation proposed by Anand *et al.* to extract values for E_a/k_B and f_0 [Eq. (9)] proved unsuccessful due to a lack of low-frequency data [39]. It is clear from these data fitting that complications exist in extracting data using the power-law, Arrhenius, and Vogel-Fulcher-type plots as has been discussed at length by Souletie and Tholence [42]. However, these data do demonstrate that the values extracted (at least from the power law) are typical of spin-glass behavior supporting the cation disorder proposed from our diffraction data.

In order to investigate the spin-glass character further we have additionally collected dc susceptibility data under a number of different conditions including variable-temperature ZFC/FC in applied magnetic fields between 2.5 mT and 7 T, ZFC hysteresis loops collected at temperatures of between 2 and 300 K, FC hysteresis loops collected at 2 K with cooling fields of between 50 mT and 3 T, as well as isothermal remnant magnetization measurements. Figure 6 gives the

ZFC/FC dc susceptibility at different applied magnetic fields. At low fields two features are clear: firstly the divergence between ZFC and FC data, labeled as feature 1 in Fig. 6(a), and a broad cusp in the ZFC data, labeled as feature 2 in Fig. 6(a). As the field increases between 2.5 and 50 mT the temperature at which these two features occur lowers and the two transitions become closer together. Increasing the applied field further results in the cusp becoming broader and less pronounced. Additionally, the divergence between the ZFC and FC data diminishes, disappearing almost completely by 7 T, suggesting that the spin-glass state is destroyed under high applied magnetic fields as expected for these types of systems [36,37]. This perhaps suggests that there may be more than one contribution to the spin-glass behavior at low applied fields. The temperature dependence of both the divergence between ZFC and FC data (feature 1 in Fig. 6) and T_f (feature 2 in Fig. 6) allows us to probe the temperature-field phase diagram and the field-dependent paramagnetic-spin-glass phase transition as shown in Fig. 6(c).

Isothermal remnant magnetization measurements were performed by cooling the $K_x\text{Ru}_{4-y}\text{Ni}_y\text{O}_8$ hollandite material in an applied magnetic field of 0.5 T (150 K \rightarrow 1.8 K) before setting the field back to zero and collecting susceptibility data

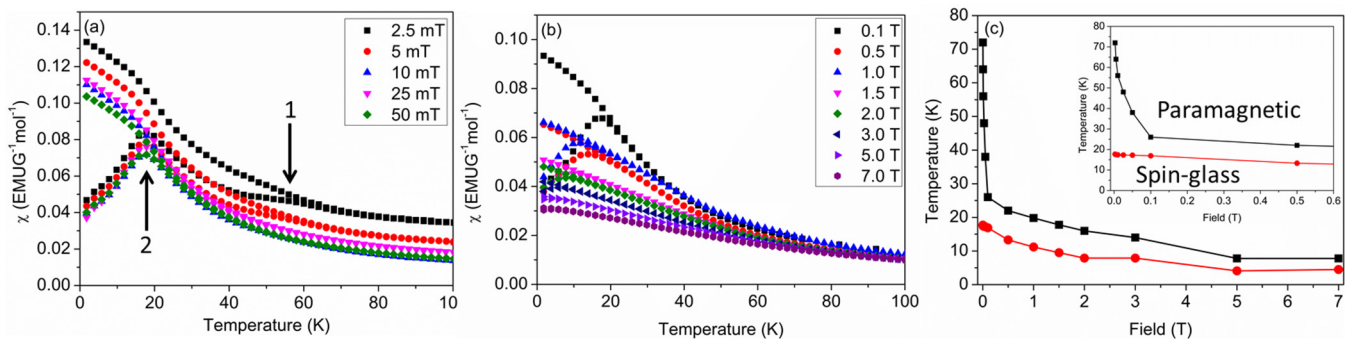


FIG. 6. dc ZFC/FC susceptibility data collected (a) between applied fields of 2.5 and 50 mT, (b) between applied fields of 0.1 and 7 T showing the shift and eventual loss of the divergence between ZFC and FC data (feature 1) and the broadening and eventual loss of the spin-glass “cusp” (feature 2). (c) Temperature-field phase diagram showing the dependence of the paramagnetic-spin-glass phase temperature on applied field where the red circles are determined from the maxima of the cusp and the black circles represent the temperature at which the divergence in ZFC/FC data occurs. The inset of (c) shows a zoomed-in portion of the low-field region of the phase diagram.

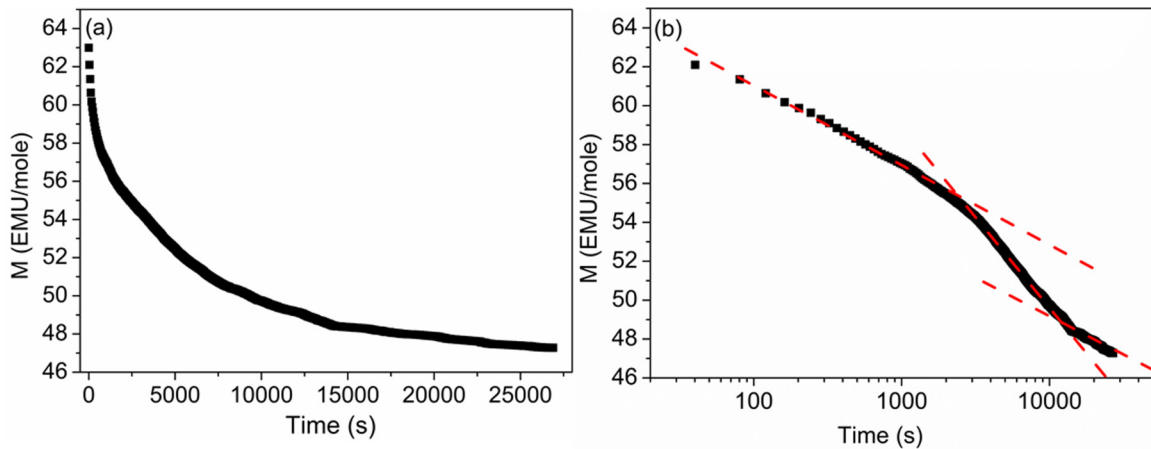


FIG. 7. Remnant magnetization decay behavior as a function of (a) time showing exponential-like decay and (b) log time showing at least three distinct components contribute to the decay behavior. Note: the dotted red lines act as a guide to the eye.

as a function of time (Fig. 7). The data show an apparent exponential decay as a function of time with the remnant magnetization remaining nonzero across the whole experiment consistent with what has been observed for other spin-glass systems [36,39]. Plotting the data on a semilogarithmic scale clearly does not give a straight line [Fig. 7(b)]. Close inspection of these data suggests at least three separate regions associated with the decay suggesting multiple components to the decay curve potentially arising as a result of either different spin correlations (i.e., Ni-Ni, Ni-Ru, Ru-Ru) and/or contributions from the RuO_2 second phase. We note, however,

that while this is in contrast with the data observed for PdNCr_3 it is more consistent with the trends observed by Anand *et al.* for PrRhSn_3 highlighting the vast differences that can be observed in spin-glass systems [36,39]. Attempts to fit these data to either a power law or exponential function of a power law as have been reported previously proved unsuccessful due to the complex nature of the decay profile [36,39].

The temperature dependence of the hysteresis behavior is shown in Fig. 8. Under ZFC conditions the degree of hysteresis weakens with increasing temperature. At 25 K only a weak deviation from linearity (“S” shape) is observed with little

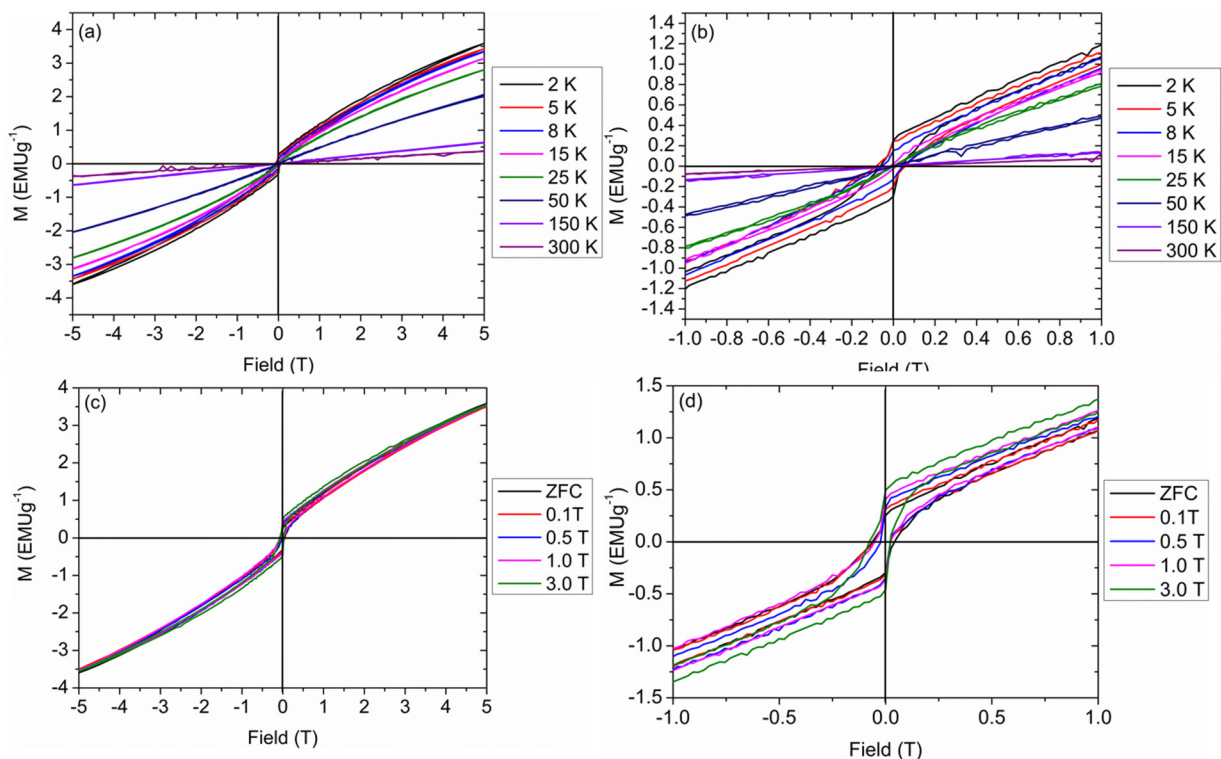


FIG. 8. (a) Zero-field-cooled hysteresis data collected at temperatures between 2 and 300 K showing the loss of hysteric behavior above ~ 50 K, (b) zoomed-in region of the data shown in (a), field-cooled hysteresis data collected at 2 K as a function of cooling field showing the increase in remnant magnetization with increasing cooling field strength, and (d) zoomed-in region of the data shown in (c).

hysteresis on variation of the field. By 50 K no hysteresis is observed with a linear response as a function of field recorded consistent with loss of spin-glass character. Hysteresis data were also collected at 2 K after field cooling from 150 K (Fig. 8). There is a clear shift in the remnant magnetization to higher values with increasing FC strength. Lin *et al.* suggested that in $PbNCr_3$ this arises as a result of the formation of larger magnetic clusters with larger applied cooling fields [36]. While this is a weaker effect in our hollandite materials it is not unreasonable to suggest that the increase in remnant magnetization observed here also arises as a result of the formation of larger spin clusters.

Overall, our susceptibility data confirm the glassy nature of $K_xRu_{4-y}Ni_yO_8$. However, it is clear that this system is far from simple with complex behavior observed in all measurements. Our refinements and spectrometry experiments suggest a potential composition of approximately $K_{0.73(3)}Ru_{2.1(5)}Ni_{1.9(5)}O_8$ giving a disordered mixture of Ni^{+3} , Ru^{+4} , and Ru^{+5} . This means that multiple possible short-range spin correlations may exist between Ni-Ni, Ni-Ru, and Ru-Ru, all of which may have different strengths and dynamics. Of course this composition is an oversimplification and we cannot rule out the possibility of oxygen vacancies and non-stoichiometry which will further complicate this system and may additionally introduce Ni^{2+} into the mix. Another point to note is that the field/temperature susceptibility dependence can also be critically dependent on the way the experiments are conducted. In order to ensure comparability in our measurements we have conducted all our experiments in the same way (ZFC/FC from 300 and 150 K in temperature- and field-dependent studies, respectively). However, while it is widely accepted that the nature of spin glasses means that there will be inherent differences between systems, differences in our data collection protocols may also limit comparison with other known spin-glass systems. Additionally, while it is expected that RuO_2 will behave as a Pauli paramagnet and thus not contribute to the spin-glass behavior of the $K_xRu_{4-y}Ni_yO_8$ hollandite material investigated here we cannot entirely rule out this possibility.

IV. CONCLUSION

In summary we report the synthesis of nickel-doped $K_xRu_4O_8$. Rietveld refinement of the x-ray diffraction data confirms that the material crystallizes with tetragonal $I4/m$ symmetry consistent with other ruthenate hollandites and cation size constraints with the nickel and ruthenium disordered across the cation site [18,19,24]. XRF spectroscopy suggests an approximate composition of

$K_{0.73(3)}Ni_{1.9(5)}Ru_{2.1(5)}O_8$. Despite the presence of RuO_2 secondary phase ($\sim 25\%$) we have been able to probe the magnetic order in the hollandite phase. We have performed a comprehensive ac and dc susceptibility study of these materials with all measurements confirming spin-glass behavior in this material. ac susceptibility data were analyzed using the power law, Arrhenius, and Vogel-Fulcher methods. The value of the relative frequency shift, δT_f , was determined as 0.025, which is within the range expected for spin-glass systems (0.005–0.06). Additionally, the characteristic flipping time of a single spin flip, τ_0 , and the dynamical critical exponent $-z\nu$ were determined to have values 5.82×10^{-8} s and 6.1(3), respectively, from the power law. While the value of τ_0 is comparatively very large, $-z\nu$ is consistent with what is expected for spin-glass systems. In contrast to the power-law treatment of these data, fits to the Vogel-Fulcher and Arrhenius equations were not successful. This is not unexpected and with respect to the Vogel-Fulcher can be linked to limited (usable) data collected at very low frequencies. The problems with these types of evaluations of ac susceptibility data have been discussed at length elsewhere [42]. Zero-field-cooled-field-cooled dc susceptibility measurements demonstrate a loss of spin-glass character with increasing magnetic field. Field-cooled hysteresis behavior demonstrates a small increase in the remnant magnetization (at 2 K) on increasing the strength of the cooling field, suggesting that the degree of short-range correlations increases consistent with the formation of larger spin clusters. Thermoremanent magnetization data indicate an exponential-like decay of the magnetization data as a function of time with the remnant magnetization remaining nonzero. However, it is clear from the $\log t$ relationship that multiple components contribute to the decay behavior observed making it difficult to gain detailed insight from these data. Overall, we suggest that the spin-glass behavior of $K_{0.73(3)}Ni_{1.9(5)}Ru_{2.1(5)}O_8$ is complex potentially arising as a result of different (strength) spin correlations (i.e., Ni-Ni, Ni-Ru, Ru-Ru) due to cation disorder and/or contributions from the RuO_2 second phase. It is clear from this study that doping ruthenium-based hollandites can lead to interesting magnetic behavior. Given the interest in $4d$ (and $5d$) magnetic systems, spin glasses, and frustrated magnetism this work may revitalize the study of magnetism in hollandite materials.

ACKNOWLEDGMENTS

We are thankful for access to the Materials Characterisation laboratories at the ISIS Muon and Neutron Source. D.C.A. is grateful to Dr. Mark Price (University of Kent) for helpful discussion.

- [1] S. Wasserman, K. Carrado, S. Yuchs, H. Cao, and S. Suib, The structure of new synthetic manganese oxide octahedral molecular-sieves, *Physica B* **208-209**, 674 (1995).
- [2] N. Duan, S. Suib, and C.-J. O'Young, Sol-gel synthesis of cryptomelane, an octahedral molecular-sieve, *J. Chem. Soc., Chem. Commun.* **0**, 1367 (1995).
- [3] Y. Shen, S. Suib, and C. J. O'Young, Effects of inorganic cation templates on octahedral molecular-sieves of manganese oxides, *J. Am. Chem. Soc.* **116**, 11020 (1994).
- [4] A. M. Larson, P. Moetakef, K. Gaskell, C. M. Brown, G. King, and E. E. Rodriguez, Inducing ferrimagnetism in insulating hollandite $Ba_{1.2}Mn_8O_{16}$, *Chem. Mater.* **27**, 515 (2015).
- [5] J. Zhang and C. W. Burnham, Hollandite-type phases: geometric consideration of unit-cell size and symmetry, *Am. Mineral.* **79**, 168 (1994).
- [6] T. Kuwabara, M. Isobe, H. Gotou, T. Yagi, D. Nishio-Hamane, and Y. Ueda, Synthesis, structure, and electromagnetic

- properties of manganese hollandite, $K_xMn_8O_{16}$, *J. Phys. Soc. Jpn.* **81**, 104701 (2012).
- [7] A. M. Larson, B. Wilfong, P. Moetakef, C. M. Brown, P. Zavalij, and E. E. Rodriguez, Metal-insulator transition tuned by magnetic field in $Bi_{1.7}V_8O_{16}$, *J. Mater. Chem. C* **5**, 4967 (2017).
- [8] P. Moetakef, A. M. Larson, B. C. Hodges, P. Zavalij, K. J. Gaskell, P. M. Piccoli, and E. E. Rodriguez, Synthesis and crystal chemistry of microporous titanates $K_x(Ti, M)_8O_{16}$ where $M = Sc-Ni$, *J. Solid State Chem.* **220**, 45 (2014).
- [9] P. Moetakef, L. Wang, A. E. Maughan, K. J. Gaskell, A. M. Larson, B. C. Hodges, and E. E. Rodriguez, Tuning the electronic band structure of microporous titanates with the hollandite structure, *J. Mater. Chem. A* **3**, 20330 (2015).
- [10] M. E. Hossain, S. Liu, S. O'Brien, and J. Li, Frequency-dependent ferroelectric behaviour of $BaMn_3Ti_4O_{14.25}$, *Appl. Phys. Lett.* **107**, 032904 (2015).
- [11] S. Liu, A. R. Akbashev, X. Yang *et al.*, Hollandites as a new class of multiferroics, *Sci. Rep.* **4**, 6203 (2014).
- [12] R. J. Cava, Schizophrenic electrons in ruthenium-based oxides, *Dalton Trans.* **19**, 2979 (2004).
- [13] Y. Maeno, H. Hashimoto, K. Yoshida, S. Nishizaki, T. Fujita, J. G. Bednorz, and F. Lichtenberg, Superconductivity in a layered perovskite without copper, *Nature (London)* **372**, 532 (1994).
- [14] Y. S. Lee, J. S. Lee, K. W. Kim, T. W. Noh, J. J. Yu, Y. Bang, M. K. Lee, and C. B. Eom, Pseudogap formation in four-layer $BaRuO_3$ and its electrodynamic response changes, *Phys. Rev. B* **64**, 165109 (2001).
- [15] Y. Tokiwa, M. Mchawat, R. S. Perry, and P. Gegenwart, Multiple Metamagnetic Quantum Criticality in $Sr_3Ru_2O_7$, *Phys. Rev. Lett.* **116**, 226402 (2016).
- [16] Y. A. Ying, K. D. Nelson, I. G. Deac, P. Schiffer, P. Khalifah, R. J. Cava, and Y. Liu, Possible observation of quantum ferromagnetic fluctuations in $La_4Ru_6O_{19}$, *Phys. Rev. B* **80**, 024303 (2009).
- [17] Z. Q. Mao, T. He, M. M. Rosario, K. D. Nelson, D. Okuno, B. Ueland, I. G. Deac, P. Schiffer, Y. Liu, and R. J. Cava, Quantum Phase Transition in Quasi-One-Dimensional $BaRu_6O_{12}$, *Phys. Rev. Lett.* **90**, 186601 (2003).
- [18] W. Kobayashi, Transport properties of quasi-one-dimensional KRu_4O_8 , *Phys. Rev. B* **79**, 155116 (2009).
- [19] M. L. Foo, W.-L. Lee, T. Siegrist, G. Lawes, A. P. Ramirez, N. P. Ong, and R. J. Cava, Electronic characterisation of alkali ruthenium hollandites: KRu_4O_8 , $RbRu_4O_8$ and $Cs_{0.8}Li_{0.2}Ru_4O_8$, *Mater. Res. Bull.* **39**, 1663 (2004).
- [20] Y. Ohta, T. Toriyama, M. Sakamaki, and T. Konishi, Anomalous electronic states of hollandite-type transition-metal oxides, *J. Phys.: Conf. Ser.* **400**, 032070 (2012).
- [21] T. Toriyama, T. Konishi, and Y. Ohta, Anomalous electronic structures of transition-metal oxides with hollandite-type crystal structure, *J. Phys.: Conf. Ser.* **391**, 012109 (2012).
- [22] T. Toriyama, M. Watanabe, T. Konishi, and Y. Ohta, Quasi-one-dimensional electronic structure of hollandite ruthenate $K_2Ru_8O_{16}$, *Phys. Rev. B* **83**, 195101 (2011).
- [23] T. Toriyama, T. Konishi, and Y. Ohta, Hollandite ruthenate $K_2Ru_8O_{16}$ as a new Tomonaga-Luttinger-liquid system, *J. Phys.: Conf. Ser.* **400**, 042063 (2012).
- [24] G. Laurita, R. Grajczyk, M. Stolt, I. Coutinho, A. W. Sleight, and M. A. Subramanian, Influence of structural disorder on hollandite $A_xRu_4O_8(A^+ = K, Rb, Rb_{1-x}Na_x)$, *Inorg. Chem.* **55**, 3462 (2016).
- [25] A. C. Larson and R. B. von Dreele, General structure Analysis System (GSAS), Los Alamos National Report LAUR, 86 (1994).
- [26] B. H. Toby, EXPGUI, a graphical user interface for GSAS, *J. Appl. Crystallogr.* **34**, 210 (2001).
- [27] P. Thompson, D. E. Cox, and J. B. Hastings, Rietveld refinement of Debye-Scherrer synchrotron x-ray data from Al_2O_3 , *J. Appl. Crystallogr.* **20**, 79 (1987).
- [28] C. J. Howard, The approximation of asymmetric neutron powder diffraction peaks by sums of Gaussians, *J. Appl. Crystallogr.* **15**, 615 (1982).
- [29] H. Miura, The crystal structure of hollandite, *Mineral J.* **13**, 119 (1986).
- [30] W. C. Hamilton, Significance tests on the crystallographic R factor, *Acta Crystallogr.* **18**, 502 (1965).
- [31] W. D. Ryden and A. W. Lawson, Magnetic susceptibility of IrO_2 and RuO_2 , *J. Chem. Phys.* **52**, 6058 (1970).
- [32] T. Berlijn, P. C. Snijders, O. Delaire, H.-D. Zhou, T. A. Maier, H.-B. Cao, S.-X. Chi, M. Matsuda, Y. Wang, M. R. Koehler, P. R. C. Kent, and H. H. Weitering, Itinerant Antiferromagnetism in RuO_2 , *Phys. Rev. Lett.* **118**, 077201 (2017).
- [33] Y. Crespo, A. Andreev, and N. Seriani, Competing antiferromagnetic and spin-glass phases in a hollandite structure, *Phys. Rev. B* **88**, 014202 (2013).
- [34] Y. Xu, S. Liu, K. Sun, X. Yu, and X. Hao, Negligible spin-orbit coupling effect in the Mott-insulating antiferromagnet $KRuO_4$, *J. Appl. Phys.* **121**, 215106 (2017).
- [35] A. P. Ramirez, Strongly geometrically frustrated magnets, *Annu. Rev. Mater. Sci.* **24**, 453 (1994).
- [36] S. Lin, D. F. Shao, J. C. Lin, L. Zu, X. C. Kan, B. S. Wang, Y. N. Huang, W. H. Song, W. J. Lu, P. Song, and Y. P. Sun, Spin-glass behavior and zero-field-cooled exchange bias in a Cr-based antiperovskite compound $PdNCr_3$, *J. Mater. Chem. C* **3**, 5683 (2015).
- [37] I. Bakaimi, R. Brescia, C. M. Brown, A. A. Tsirlin, M. A. Green, and A. Lappas, Hydration-induced spin-glass state in a frustrated Na-Mn-O triangular lattice, *Phys. Rev. B* **93**, 184422 (2016).
- [38] H. Khurshid, P. Lampen-Kelley, O. Iglesias, J. Alonso, M.-H. Phan, C.-J. Sun, M.-L. Saboungi, and H. Srikanth, Spin-glass-like freezing of inner and outer surface layers in hollow $\gamma-Fe_2O_3$ nanoparticles, *Sci. Rep.* **5**, 15054 (2015).
- [39] V. K. Anand, D. T. Adroja, and A. D. Hillier, Ferromagnetic cluster spin-glass behavior in $PrRhSn_3$, *Phys. Rev. B* **85**, 014418 (2012).
- [40] J. Yu, S. Tang, L. Wang, and Y. Du, Spin-glass-like behaviour in hollandite $Ba_{1+\delta}Mn_8O_{16}$ nanoribbons synthesized by molten-salt method, *Chem. Phys. Lett.* **496**, 117 (2010).
- [41] A. Rotaru, D. C. Arnold, A. Daoud-Aladine, and F. D. Morrison, Origin and stability of the dipolar response in a family of tetragonal tungsten bronze relaxors, *Phys. Rev. B* **83**, 184302 (2011).
- [42] J. Souletie and J. L. Tholence, Critical slowing down in spin-glasses and other glasses - Fulcher versus Power Law, *Phys. Rev. B* **32**, 516 (1985).